Properties of toroidal Alfvén eigenmode in DIII-D plasma

Zhixuan Wang,[1] Zhihong Lin,[1,a)] Wenjun Deng,[2] Ihor Holod,[1] W. W. Heidbrink,[1] Y. Xiao,[3] H. Zhang,[4] W. Zhang,[5,b)] and M. Van Zeeland[6]
[1]*University of California, Irvine, California 92697, USA*
[2]*Princeton Plasma Physics Laboratory, Princeton, New Jersey 08543-0451, USA*
[3]*Institute for Fusion Theory and Simulation, Zhejiang University, Hangzhou, Zhejiang 310058, China*
[4]*Fusion Simulation Center, Peking University, Beijing 100871, China*
[5]*Institute of Physics, Chinese Academy of Sciences, Beijing 100190, China*
[6]*General Atomics, San Diego, California 92121, USA*

(Received 28 August 2014; accepted 30 January 2015; published online 19 February 2015)

Linear properties of the toroidal Alfvén eigenmode (TAE) excited by energetic particles (EP) in a DIII-D tokamak experiment have been studied in global gyrokinetic particle simulations treating self-consistently kinetic effects of EP, thermal ions, and electrons. Simulation results of the TAE frequency and mode structure agree very well with the experimental measurements. The non-perturbative EP contribution induces a radial localization of the TAE mode structure, a break-down of mode radial symmetry, as well as a frequency dependence on the toroidal mode number. The simulations further demonstrate the dependence of the growth rate and mode structure on EP pressure gradients. The in-out asymmetry of the mode structure and the experimental identification of the poloidal harmonics have also been clarified. © *2015 AIP Publishing LLC*.
[http://dx.doi.org/10.1063/1.4908274]

I. INTRODUCTION

In tokamaks, numerous discrete shear Alfvén eigenmodes have been found in the gaps of the continuous Alfvén spectrum produced by the toroidal geometry,[1,2] acoustic coupling,[3,4] etc. These weakly damped modes can be easily destabilized in the presence of energetic particles (EP),[5–8] generated either by fusion products or by auxillary heating such as neutral beam injection (NBI). While it has been shown both numerically[9–11] and experimentally[12–14] that the transport of energetic particles by ion temperature gradient microturbulence is usually insignificant, these unstable Alfvén eigenmodes, especially the toroidicity-induced Alfvén eigenmode (TAE), have been found to induce large cross-field transport of energetic particles,[7,8,12,15–18] which leads to a degradation of the overall plasma confinement, and possible serious damage of the first-wall components.

The energetic particle transport induced by nonlinear dynamics of Alfvén instabilities may depend on both kinetic and magnetohydrodynamic (MHD) physics. The complicated nature of this issue requires a nonlinear global gyrokinetic simulation. Recently, gyrokinetic simulations treating non-perturbatively the dynamics of both EP and thermal plasmas have been verified and validated[19] for the reversed shear Alfvén eigenmode in the DIII-D discharge No. 142111 (Ref. 16) at 725 ms. Several gyrokinetic codes have been applied to simulate the EP-driven TAE. Lauber *et al.*[20,21] have developed a global gyrokinetic eigenvalue code LIGKA. Lang *et al.*[22] and Chen *et al.*[23] have extended the GEM code for both low-n and high-n TAE simulations with fluid electrons (n is the toroidal mode number). Mischenko *et al.*[24,25] used δf particle-in-cell code GYGLES to demonstrate EP and bulk plasma pressure effects on TAE. Bass and Waltz have investigated the nonlinear saturation of high-n TAE and its associated EP transport with the flux-tube simulation from GYRO.[26,27]

Here, we apply the gyrokinetic toroidal code (GTC)[28] to study the physics of TAE. GTC has been successfully applied to simulate transport by microturbulence,[29,30] linear[31–35] and nonlinear[36,37] dynamics of Alfvén eigenmodes. GTC simulations of TAE have been carried out since Nishimura *et al.*[38] W. Zhang *et al.*[33] have observed the excitation of TAE by EP and by antenna. C. Zhang *et al.*[39] have further studied the transition from EP-driven TAE to energetic particle mode (EPM). The most recent GTC simulation[40] has shown a radial localization of TAE in the DIII-D discharge No. 142111 at 525 ms. This finding is important both conceptually and practically. Conceptually, the localization is beyond the conventional paradigm of the MHD theory with a perturbative treatment of the EP dynamics and blurs the boundary between the Alfvén eigenmodes and the energetic particle modes.[5] Practically, the radial localization could have profound implications on the EP transport. The radial mode width is one of the important factors determining the EP transport level. The TAE radial drift could induce convective or even avalanche-like EP transport similar to that of the energetic particle modes.[41]

In the current work, we further investigate the effect of the non-perturbative EP drive on TAE and linear properties of TAE in the DIII-D experiment No. 142111 at 525 ms. In addition to the radial localization, we find the radial and

a)Author to whom the correspondence should be addressed. Electronic mail: zhihongl@uci.edu.
b)Also at: Department of Modern Physics, University of Science and Technology of China, Hefei 230026, China.

poloidal asymmetry of the mode structure, and TAE frequency dependence on the toroidal mode number. A scan of the strength of the EP drive shows a shift of mode structure when the EP pressure changes.

This paper is organized as follows: GTC simulation model is described in Sec. II. We show that ideal MHD result, in particular, the dispersion relation of TAE, can be recovered in this model. In Sec. III, linear simulation results of TAE are discussed. In Sec. IV, we present the results of two scans on the EP pressure. Conclusions and discussions are in Sec. V.

II. GTC SIMULATION MODEL

In this section, we first describe the electromagnetic models to treat different species. Then we show that when kinetic effects are artificially turned off in the long-wavelength limit, the formulation is reduced to the ideal MHD theory. Finally, the TAE dispersion relation is derived from the reduced equations.

A. Nonlinear gyrokinetic model for ion and EP

Ion and EP species in GTC are described by the nonlinear gyrokinetic equations[42–44] retaining the finite Larmor radius effects. In this work, we choose the δf method because we will focus only on the linear properties of TAE, although GTC is capable of both δf and full-f simulations. Decomposing the quantities into time-independent equilibrium and time-dependent perturbed components, we can write the gyrokinetic equation

$$(\partial_t + \dot{\boldsymbol{X}}\cdot\nabla + \dot{v}_\parallel\partial_{v_\parallel})[f_{0\alpha}(\boldsymbol{X},\mu,v_\parallel) + \delta f_\alpha(\boldsymbol{X},\mu,v_\parallel,t)] = 0, \tag{1}$$

$$\dot{\boldsymbol{X}} = v_\parallel\frac{\boldsymbol{B}_0 + \langle\delta\boldsymbol{B}\rangle}{B_0} + \boldsymbol{v}_E + \boldsymbol{v}_c + \boldsymbol{v}_g, \tag{2}$$

$$\dot{v}_\parallel = -\frac{1}{m_\alpha}\frac{\boldsymbol{B}^*}{B_0}\cdot(\mu\nabla B_0 + Z_\alpha\nabla\delta\langle\phi\rangle) - \frac{Z_\alpha}{m_\alpha c}\partial_t\langle\delta A_\parallel\rangle. \tag{3}$$

The subscripts $\alpha = e, i, f$ stand for particle species, electron e, thermal ion i, and fast ion (also called energetic particle) f; Z_α, m_α, and Ω_α are their corresponding electric charge, mass, and cyclotron frequency, respectively. $\boldsymbol{X}, v_\parallel$, and μ denote the coordinate of the 5D phase space, which are the gyro-center position, the parallel velocity, and the magnetic moment, respectively. The $\boldsymbol{E}\times\boldsymbol{B}$ drift velocity $\boldsymbol{v}_E$, the magnetic curvature drift velocity $\boldsymbol{v}_c$, and the grad-B drift velocity $\boldsymbol{v}_g$ are given by

$$\boldsymbol{v}_E = \frac{c\boldsymbol{b}_0\times\nabla\langle\delta\phi\rangle}{B_0}, \tag{4}$$

$$\boldsymbol{v}_c = \frac{v_\parallel^2}{\Omega_\alpha}\nabla\times\boldsymbol{b}_0, \tag{5}$$

$$\boldsymbol{v}_g = \frac{\mu}{m_\alpha\Omega_\alpha}\boldsymbol{b}_0\times\nabla B_0. \tag{6}$$

$\langle F\rangle$ denotes the gyro-averaging of any function F over the gyroangle θ_c

$$\langle F\rangle(\boldsymbol{X},\ldots) \equiv \int\frac{d\theta_c}{2\pi}F\big[\boldsymbol{X} + \boldsymbol{\rho}\big(\boldsymbol{X},\mu,v_\parallel,\theta_c\big),\ldots\big], \tag{7}$$

where $\boldsymbol{\rho}$ is the gyro-radius vector pointing from the gyrocenter position to the particle position.

$\boldsymbol{B}_0$, $\delta\boldsymbol{B}$, $\delta\phi$, and $\delta A_\parallel$ denote the equilibrium and the perturbed magnetic field, the perturbed electrostatic potential, and the perturbed parallel vector potential, respectively. $\boldsymbol{B}^*$ is given by

$$\boldsymbol{B}^* \equiv \boldsymbol{B}_0 + \frac{B_0 v_\parallel}{\Omega_\alpha}\nabla\times\boldsymbol{b}_0 + \langle\delta\boldsymbol{B}\rangle, \tag{8}$$

where $\boldsymbol{b}_0 \equiv \boldsymbol{B}_0/B_0$ is the direction of the equilibrium magnetic field. We ignore the parallel perturbed magnetic field $\delta B_\parallel$ for low-β plasmas (β is the ratio of kinetic to magnetic pressure), so the perturbed magnetic field can be completely determined by $\delta A_\parallel$ alone

$$\delta\boldsymbol{B} = \delta\boldsymbol{B}_\perp \equiv \nabla\times(\delta A_\parallel\boldsymbol{b}_0). \tag{9}$$

The electrostatic potential $\delta\phi$ is calculated by the gyrokinetic Poisson equation[43]

$$\frac{Z_i^2 n_i}{T_i}\big(\delta\phi - \delta\tilde{\phi}\big) = \Sigma_\alpha Z_\alpha\delta n_\alpha, \tag{10}$$

where

$$\delta n_\alpha = \int_{GC}\delta f_\alpha d\boldsymbol{v} \quad \text{for each species}, \quad \delta\tilde{\phi} = \frac{1}{n_i}\int_{GC} f_{0i}\langle\langle\delta\phi\rangle\rangle d\boldsymbol{v}. \tag{11}$$

Here, $\int_{GC}d\boldsymbol{v} \equiv \frac{2\pi B}{m_\alpha}\int d\mu dv_\parallel$ is the integral over the gyrocenter velocity space.[43]

B. Fluid-kinetic hybrid model for electrons

In order to improve the numerical properties of electrons for Alfvén eigenmode simulation, we adopt, in this work, the fluid-kinetic hybrid electron model,[45] which expand the electron response by the order of a small parameter associated with the electron to ion mass ratio, i.e., $\omega/k_\parallel v_\parallel$, for the non-zonal mode.[44] The lowest order adiabatic electrons are described by the fluid equations, which remove numerical difficulties associated with the collisionless tearing modes and the electron Courant condition that greatly limit the simulation time step size. The higher order nonadiabatic response is treated kinetically with all the kinetic effects preserved.

1. Electron fluid equations

We calculate the perturbed electron density through the electron continuity equation, which is obtained by integrating the electron drift-kinetic equation ($k_\perp\rho_e \to 0$ limit of Eq. (1)) over the velocity space. It reads[35]

$$0=\partial_t\delta n_e+\boldsymbol{B}_0\cdot\nabla\left(\frac{n_{0e}\delta u_{\parallel e}}{B_0}\right)+B_0\boldsymbol{v}_E\cdot\nabla\left(\frac{n_{0e}}{B_0}\right)$$
$$-n_{0e}\left(\delta\boldsymbol{v}_e^*+\boldsymbol{v}_E\right)\cdot\frac{\nabla B_0}{B_0}+\delta\boldsymbol{B}\cdot\nabla\left(\frac{n_{0e}u_{\parallel 0e}}{B_0}\right)$$
$$+\frac{c\nabla\times\boldsymbol{B}_0}{B_0^2}\cdot\left[-\frac{\nabla\delta P_{\parallel e}}{e}-\frac{\left(\delta P_{\perp e}-\delta P_{\parallel e}\right)\nabla B_0}{eB_0}+n_{0e}\nabla\delta\phi\right]$$
$$+\delta\boldsymbol{B}\cdot\nabla\left(\frac{n_{0e}\delta u_{\parallel e}}{B_0}\right)+\boldsymbol{B}_0\boldsymbol{v}_E\cdot\nabla\left(\frac{\delta n_e}{B_0}\right)$$
$$+\frac{c\delta n_e}{B_0^2}\boldsymbol{b}_0\times\nabla B_0\cdot\nabla\delta\phi+\frac{c\delta n_e}{B_0^2}\nabla\times\boldsymbol{B}_0\cdot\nabla\delta\phi. \tag{12}$$

Here, $u_{\parallel 0e}$, $\delta u_{\parallel}$, $\delta P_{\parallel e}$, and $\delta P_{\perp e}$ are the equilibrium and perturbed fluid veolcity, perturbed electron parallel and perpendicular pressure, etc., defined as

$$u_{\parallel 0e}=\int_{GC}f_{0e}v_{\parallel}d^3\boldsymbol{v}/n_{0e}, \tag{13}$$
$$\delta u_{\parallel e}=\int_{GC}\delta f_e v_{\parallel}d^3\boldsymbol{v}/n_{0e}, \tag{14}$$
$$\delta P_{\parallel e}=\int_{GC}\delta f_e v_{\parallel}^2 d^3\boldsymbol{v}, \tag{15}$$
$$\delta P_{\perp e}=\int_{GC}\delta f_e v_{\perp}^2 d^3\boldsymbol{v}=B_0\int_{GC}\delta f_e\mu d^3\boldsymbol{v}. \tag{16}$$

In this work, we only keep the linear terms in the first three lines. Then, $\delta u_{\parallel e}$ is calculated by Ampère's law in the limit of $k_{\parallel}\ll k_{\perp}$

$$-\frac{c}{4\pi}\nabla_{\perp}^2\delta A_{\parallel}=\Sigma_{\alpha}\delta J_{\parallel\alpha}\Rightarrow en_{0e}\delta u_{\parallel e}=\frac{c}{4\pi}\nabla_{\perp}^2\delta A_{\parallel}+\Sigma_{\alpha=i,f}\delta J_{\parallel\alpha}, \tag{17}$$

where $\delta J_{\parallel\alpha}=\int_{GC}Z_{\alpha}v_{\parallel}\delta f_{\alpha}d\boldsymbol{v}$ for each species.

We use effective potential ϕ_{eff} to represent the parallel electric field

$$\delta E_{\parallel}=-\boldsymbol{b}_0\cdot\nabla\delta\phi_{\text{eff}}. \tag{18}$$

So $\partial_t\delta A_{\parallel}$ is given by the parallel gradient of the inductive potential $\delta\phi_{\text{ind}}\equiv\delta\phi_{\text{eff}}-\delta\phi$,

$$\partial_t\delta A_{\parallel}=c(\delta E_{\parallel}+\boldsymbol{b}_0\cdot\nabla\delta\phi)$$
$$=-c\boldsymbol{b}_0\cdot\nabla(\delta\phi_{\text{eff}}-\delta\phi)=-c\boldsymbol{b}_0\cdot\nabla\delta\phi_{\text{ind}}. \tag{19}$$

Note that the $k_{\parallel}=0$ component of inductive $\delta E_{\parallel}$ is ignored here (i.e., collisionless tearing mode is removed).

In order to calculate the $\delta\phi_{\text{eff}}$, we expand the electron response in the order of the small number $\omega/k_{\parallel}v_{\parallel}$. We separate the electron distribution function into equilibrium and perturbed components, $f_e=f_{0e}+\delta f_e$. The perturbed distribution function is further separated into adiabatic and nonadiabatic parts,

$$\delta f_e=\delta f_e^{(0)}+\delta h_e, \tag{20}$$

where the lowest adiabatic response $\delta f_e^{(0)}$ is defined as the solution of the lowest order of Eq. (1) in the limit of $m_e\to 0$ (or equivalently $v_{\parallel}\to\infty$).

$$v_{\parallel}\boldsymbol{b}_0\cdot\nabla|_{v_{\perp}}\delta f_e^{(0)}=-v_{\parallel}\frac{\delta\boldsymbol{B}}{B_0}\cdot\nabla|_{v_{\perp}}f_{0e}+v_{\parallel}\frac{f_{0e}e}{T_e}\boldsymbol{b}_0\cdot\nabla\delta\phi_{\text{eff}}. \tag{21}$$

Using the Clebsch representation of the toroidal magneitc fileds,

$$\boldsymbol{B}=\boldsymbol{B}_0+\delta\boldsymbol{B}=\nabla(\psi+\delta\psi)\times\nabla(\alpha+\delta\alpha), \tag{22}$$

and assuming that the equilibrium distribution function is uniform along the background field $\boldsymbol{b}_0\cdot\nabla f_0=0$ (i.e., ignoring neoclassical effects), we can find the solution of Eq. (21)

$$\delta f_e^{(0)}=\frac{e\delta\phi_{\text{eff}}}{T_e}f_{0e}+\left.\frac{\partial f_{0e}}{\partial\psi}\right|_{v_{\perp}}\delta\psi+\left.\frac{\partial f_{0e}}{\partial\alpha}\right|_{v_{\perp}}\delta\alpha, \tag{23}$$

or equivalently,

$$\frac{e\delta\phi_{\text{eff}}}{T_e}=\frac{\delta n_e}{n_{0e}}-\frac{\delta\psi}{n_0}\frac{\partial n_0}{\partial\psi}-\frac{\delta\alpha}{n_0}\frac{\partial n_0}{\partial\alpha}. \tag{24}$$

Eqs. (10), (12), (17), (19), and (24), together with the ion contribution, form a closed nonlinear system in the lowest order of electron-ion mass ratio expansion.

2. Kinetic equation for electron nonadiabatic response

The higher-order correction to the lowest-order adiabatic response of electrons is defined as $\delta h_e\equiv\delta f_e-\delta f_e^{(0)}$ and $w_e=\delta h_e/f_e$. The $(l+1)$ th order correction to the evolution of δh_e is still determined by Eq. (1) with the lth order response $\delta f_e^{(l)}$

$$\mathcal{L}_0\delta h_e^{(l+1)}=-\delta\mathcal{L}^{(l)}f_{0e}-\mathcal{L}_0\delta f_e^{(l)}, \tag{25}$$

where propagators $\mathcal{L}_0$ and $\delta\mathcal{L}$ are defined as

$$\mathcal{L}_0=\frac{\partial}{\partial t}+\left(v_{\parallel}\boldsymbol{b}_0+\boldsymbol{v}_c+\boldsymbol{v}_g\right)\cdot\nabla-\frac{\mu}{m_e}\frac{\boldsymbol{B}_0^*}{B_0}\cdot\nabla B_0\frac{\partial}{\partial v_{\parallel}}, \tag{26}$$

$$\delta\mathcal{L}=\left(v_{\parallel}\frac{\delta\boldsymbol{B}}{B_0}+\boldsymbol{v}_E\right)\cdot\nabla-\frac{1}{m_e}\left[\frac{\delta\boldsymbol{B}}{B_0}\cdot\nabla B_0-e\frac{\boldsymbol{B}_0^*}{B_0}\cdot\nabla\delta\phi-\frac{e}{c}\frac{\partial}{\partial t}\delta A_{\parallel}\right]\frac{\partial}{\partial v_{\parallel}}. \tag{27}$$

So, δh_e can be calculated iteratively with the corrected parallel effective potential, starting from adiabatic response Eq. (24)

$$\frac{dw_e}{dt}^{(l+1)}=\frac{1}{f_e}\frac{dh_e}{dt}^{(l+1)}=\frac{f_{0e}}{f_e}\frac{1}{f_{0e}}\left[-\mathcal{L}_0\delta f_e^{(0)}-\delta\mathcal{L}f_{0e}\right]$$
$$=\left(1-\frac{\delta f_e^{(0)}}{f_{0e}}-w_e^{(l)}\right)\left[-\boldsymbol{v}_E\cdot\nabla\ln f_{0e}\Big|_{v_{\perp}}-\left.\frac{\partial f_0}{\partial\psi_0}\right|_{v_{\perp}}\frac{\partial\delta\psi}{\partial t}-\left.\frac{\partial f_0}{\partial\alpha_0}\right|_{v_{\perp}}\frac{\partial\delta\alpha}{\partial t}-\frac{1}{f_{0e}}\frac{\partial\delta f_e^{(0)}}{\partial t}-\boldsymbol{v}_d\cdot\nabla\left(\frac{\delta f_e^{(0)}}{f_{0e}}-\delta\phi\right)\right], \tag{28}$$

where the adiabatic response $\delta f_e^{(0)}$ is updated in each iteration by the update of $\delta\phi_{\rm eff}$ in its definition, Eq. (23),

$$\delta\phi_{\rm eff}^{(l+1)} = \delta\phi_{\rm eff}^{(0)} - \frac{T_e}{en_{0e}}\int_{GC}\delta h_e^{(l+1)}d^3\boldsymbol{v}. \tag{29}$$

The kinetic equation above can be used to calculate the wave-particle interaction. Since the main mechanism for wave-electron interaction is the parallel and precessional resonances in the case of Alfvén eigenmodes in tokamaks, we only need to resolve the dynamics of low-speed electrons with the parallel velocity similar to the Alfvén velocity and those with the precessional frequency similar to the wave frequency, rather than the non-resonent electrons, most of which have a velocity around the electron thermal velocity. Note that thermal electrons also carry the perturbed non-resonant density and current that give rise to the shear Alfvén wave.[45] This non-resonant density and current are already accounted for in the fluid electron equations, so it is not required resolving the dynamics of the thermal electrons in the hybrid model. Nonetheless, we still need to calculate the electron orbits accurately for the precessional resonance. This is done by using electron sub-cycling, where electron orbits are updated several times for each update of ion orbits and perturbed fields.

In this work, convergence test suggests that the simulation result converges very well when this hybrid model is solved up to the second order. So, all the results shown in this paper including kinetic electrons are solved up to the second order.

C. TAE dispersion relation

It has been shown in Ref. 34 that in the linear and long wavelength fluid limit, the gyrokinetic formulation described above reduces to the ideal MHD eigenmode equation

$$\begin{aligned}0 = &\frac{\omega(\omega-\omega_{*P})}{v_A^2}\nabla_\perp^2\delta\phi + i\boldsymbol{B}_0\cdot\nabla\left[\frac{\nabla_\perp^2(k_\parallel\delta\phi)}{B_0}\right]\\ &-i\nabla(k_\parallel\delta\phi)\times\boldsymbol{b}_0\cdot\left(\frac{\boldsymbol{b}_0\cdot\nabla\times\boldsymbol{B}_0}{B_0}\right)\\ &-i\omega\frac{4\pi}{c}\nabla\cdot\left(\frac{\boldsymbol{b}_0}{B_0}\times\nabla\cdot\delta\mathbb{P}\right),\end{aligned} \tag{30}$$

where the diamagnetic angular frequency ω_{*P}, the Alfvén velocity v_A, and the perturbed pressure tensor $\delta\mathbb{P}$ are given by

$$\omega_{*P} = -i\frac{c\boldsymbol{b}_0\times\nabla P_{0i}}{Z_iB_0n_{0i}}\cdot\nabla, \tag{31}$$

$$v_A = \frac{B_0}{\sqrt{4\pi n_{0i}m_i}}, \tag{32}$$

$$\delta\mathbb{P} = \Sigma_\alpha\int_{GC}\delta f_\alpha\boldsymbol{v}\boldsymbol{v}d^3\boldsymbol{v}. \tag{33}$$

If we adopt the assumption that $\omega_{*P}\ll\omega$, $k_\perp L_{\rm eq}\gg 1$, where $L_{\rm eq}$ is the equilibrium nonuniformity scale length, Eq. (30) can be simplified to

$$\frac{\omega^2}{v_A^2}\nabla_\perp^2\delta\phi + \boldsymbol{B}_0\cdot\nabla\left[\frac{1}{B_0}\nabla_\perp^2(\boldsymbol{b}_0\cdot\nabla\delta\phi)\right] = 0. \tag{34}$$

The equilibrium field $\boldsymbol{B}_0$ is described by the contravariant representation $\boldsymbol{B}_0\equiv\nabla\alpha\times\nabla\psi$, where $\alpha=\zeta-q(\psi)\theta$ is the magnetic field line label in a toroidal system and q is the safety factor. The covariant form reads $\boldsymbol{B}_0=\delta\nabla\psi+I(\psi)\nabla\theta+g(\psi)\nabla\zeta$. Thus, $\boldsymbol{B}_0\cdot\nabla=\mathcal{J}^{-1}(\partial_\theta+q\partial_\zeta)$, with $\mathcal{J}\equiv(gq+I)/B_0^2$ being the Jacobian.[44] Now, Eq. (34) becomes

$$\mathcal{J}^{-1}\left(\frac{\partial}{\partial\theta}+q\frac{\partial}{\partial\zeta}\right)\left[\frac{1}{\mathcal{J}B_0^2}\nabla_\perp^2\left(\frac{\partial}{\partial\theta}+q\frac{\partial}{\partial\zeta}\right)\delta\phi\right]+\frac{\omega^2}{v_A^2}\nabla_\perp^2\delta\phi=0. \tag{35}$$

Note that q, $g/(B_aR_0)=1+\mathcal{O}(\epsilon^2)$, $I/(B_aR_0)=\mathcal{O}(\epsilon^2)$ are all flux functions which do not depend on θ, and $B_0=B_a/(1+\epsilon\cos\theta)+\mathcal{O}(\epsilon^2)$ with B_a being the on-axis magnetic field.[35] Here, $\epsilon\equiv r/R_0$ is the inverse aspect ratio. We can further simplify the equation to the form

$$\begin{aligned}&\left(\frac{\partial}{\partial\theta}+q\frac{\partial}{\partial\zeta}\right)\left[\nabla_\perp^2\left(\frac{\partial}{\partial\theta}+q\frac{\partial}{\partial\zeta}\right)\delta\phi\right]\\ &\quad+\Omega^2(1+4\epsilon\cos\theta)\nabla_\perp^2\delta\phi=0,\end{aligned} \tag{36}$$

where $\Omega^2\equiv q^2R_0^2(\omega^2/B_a^2)(B_0^2/v_A^2)$ is a constant.

From the expected TAE mode structures, we bring in two assumptions here for high toroidal mode number n. First, we suppose that all poloidal harmonics are localized at its mode rational surface $q(\psi_m)=m/n$. Then, we assume that the equilibrium properties barely change between the neighbouring mode rational surfaces; thus, the poloidal m-harmonic component of the eigenfunction $\delta\phi_m$ is approximately translational invariant (i.e., radial symmetry, or mathematically, $\delta\Phi(nq(\psi_m+\Delta\psi)-m)\equiv\delta\phi_m(\psi_m+\Delta\psi)\approx\delta\phi_{m+1}(\psi_{m+1}+\Delta\psi)\equiv\delta\Phi(nq(\psi_{m+1}+\Delta\psi)-(m+1))$, where $\Delta\psi$ is the distance from the mode rational surface ψ_m). With these two assumptions, now we can write the eigenfunction of TAE of a single toroidal mode number n using ballooning mode formulas

$$\begin{aligned}\delta\phi(\boldsymbol{r},t) &= e^{i(n\zeta-\omega t)}\sum_m\delta\phi_m(\psi)e^{-im\theta}+c.c.\\ &= e^{i(n\zeta-\omega t)}\sum_m\delta\Phi(nq(\psi)-m)e^{-im\theta}+c.c.\end{aligned} \tag{37}$$

With this form, the eigenmode equation becomes a differential-difference equation

$$\begin{aligned}0 = &i\mathcal{Q}[\nabla_\perp^2 i\mathcal{Q}(\delta\Phi(\mathcal{Q})e^{-im\theta})]+\Omega^2\delta\Phi(\mathcal{Q})e^{-im\theta}\\ &+2\Omega^2\epsilon\nabla_\perp^2[e^{-im\theta}(\delta\Phi(\mathcal{Q}-1)+\delta\Phi(\mathcal{Q}+1))].\end{aligned} \tag{38}$$

Here, $\mathcal{Q}\equiv nq-m$. Now, if we define the Fourier transform of $\delta\Phi$

$$\delta\hat{\Phi}(\eta)\equiv\int_{-\infty}^{\infty}\delta\Phi(\mathcal{Q})e^{i(\mathcal{Q})\eta}d\mathcal{Q}=\mathcal{F}[\delta\Phi(\mathcal{Q})], \tag{39}$$

where η can be seen as the generalized poloidal angle along the magnetic field line, then we get the Fourier transform of the eigenmode equation

$$0 = \frac{d}{d\eta}\left[\left(1+\hat{s}^2\eta^2\right)\frac{d}{d\eta}\delta\hat{\Phi}\right] + \Omega^2(1+4\epsilon\cos\eta)\left(1+\hat{s}^2\eta^2\right)\delta\hat{\Phi}, \tag{40}$$

with the magnetic shear defined as $\hat{s} \equiv (dq/dr)(r/q)$, because

$$e^{im\theta}\mathcal{F}\left[\nabla_\perp^2\left(\delta\Phi e^{-im\theta}\right)\right] = \mathcal{F}\left[\left(\frac{\partial^2}{\partial r^2} - \frac{m^2}{r^2}\right)\delta\Phi\right] = \frac{m^2}{r^2}\left(1+\hat{s}^2\eta^2\right)\delta\hat{\Phi}(\eta), \tag{41}$$

$$\mathcal{F}[\delta\Phi(\mathcal{Q}-1) + \delta\Phi(\mathcal{Q}+1)] = 2\cos(\eta)\delta\hat{\Phi}(\eta). \tag{42}$$

The final form is the high-n ballooning eigenmode equation

$$\left[\frac{d^2}{d\eta^2} + \Omega^2(1+4\epsilon\cos\eta) - \frac{\hat{s}^2}{\left(1+\hat{s}^2\eta^2\right)^2}\right]\delta\Psi = 0, \tag{43}$$

where $\delta\Psi \equiv \sqrt{1+\hat{s}^2\eta^2}\,\delta\hat{\Phi}$. Boundary condition for this ordinary differential equation is given by $\lim_{|\eta|\to\infty}\delta\Psi = 0$.

Following previous work,[1,2,46,47] we can solve this equation in two regions and then match them asymptotically. First, we consider the outer region $|\eta| \gg 1$. In this region, Eq. (43) reduces to the standard Mathieu's equation, which gives a gap at $\Omega^2 \approx 1/4$. The lowest order solution in this outer region is simply

$$\delta\Psi_{\text{out}} = A_o e^{-\gamma|\eta|}\left[\cos\left(\frac{\eta}{2}\right) + \sqrt{-(\Gamma_+/\Gamma_-)}\sin\left(\frac{\eta}{2}\right)\right]. \tag{44}$$

Here, we have

$$\gamma \equiv \sqrt{-\Gamma_+\Gamma_-} \quad \text{and} \quad \begin{cases} \Gamma_- \equiv \Omega^2 - \Omega_u^2 \\ \Gamma_+ \equiv \Omega^2 - \Omega_l^2, \end{cases} \tag{45}$$

with Ω_u, Ω_l defined as

$$\Omega_u^2 \equiv \frac{1}{4(1-2\epsilon)}, \quad \Omega_l^2 \equiv \frac{1}{4(1+2\epsilon)}. \tag{46}$$

Then, we consider the region $|\eta| \sim \mathcal{O}(1)$, in which $4\Omega^2\epsilon\cos\eta \ll \hat{s}^2/(1+\hat{s}^2\eta^2)^2$. The lowest order solution is given by

$$\delta\Psi_{\text{in}} = A_i\left[\cos\left(\frac{\eta}{2}\right) + \frac{\hat{s}}{2}\left(\frac{\hat{s}\eta}{1+\hat{s}^2\eta^2} + \arctan(\hat{s}\eta)\right)\sin\left(\frac{\eta}{2}\right)\right]. \tag{47}$$

Now, we match the inner and the outer solution, $\lim_{\eta\to\infty}\delta\Psi_{\text{in}} = \lim_{\eta\to 0}\delta\Psi_{\text{out}}$. This gives us the eigenvalue ω by solving the following simple algebra equation

$$\sqrt{\frac{\Omega^2-\Omega_l^2}{\Omega_u^2-\Omega^2}} = \frac{|\hat{s}|\pi}{4} \Rightarrow 1-\epsilon < \frac{\omega}{\omega_A} < 1+\epsilon, \tag{48}$$

with $\omega_A \equiv v_{A0}/(2qR_0)$.

This solution gives the lower and upper bounds of the continuous spectra, which have a gap width of $2\epsilon\omega_A$.[33]

III. MODE STRUCTURE

The equilibrium geometry and the plasma profiles used in the simulations are all taken from the experimental equilibrium data at 525(ms) of DIII-D shot No. 142111, constructed by EFIT[48] and ONETWO.[49] The equilibrium radial profiles are shown in Ref. 40. The magnetic shear is weakly reversed. In the radial range of interest ($\rho = 0.4 \sim 0.7$), the distances between neighbouring mode rational surfaces are about 3 cm for $\mathtt{n}=4$ TAE, while the equilibrium scale lengths for thermal species are all over 20 cm. Thus, the assumption needed for the validity of the ballooning representation (Eq. (37)) is satisfied. The dominant TAE drive is the EP density gradients. The on-axis density and temperature are $(n_f = 2.93\times10^{12}(\text{cm}^{-3}), T_f = 24.5(\text{keV}))$ for EP, $(n_i = 2.65\times10^{13}(\text{cm}^{-3}), T_i = 1.64(\text{keV}))$ for thermal ions, and $(n_e = 2.99\times10^{13}(\text{cm}^{-3}), T_e = 2.05(\text{keV}))$ for electrons. At the steepest EP density gradient, $L_{T,EP} = 1/(d\ln(T_f)/dr) \approx 52(\text{cm})$ and $L_{n,EP} = 1/(d\ln(n_f)/dr) \approx 9.8(\text{cm})$. The on-axis magnetic field is $B_a = 1.94(\text{T})$. The on-axis ratio of the plasma pressure to the magnetic pressure is $\beta = \beta_e + \beta_i + \beta_{EP} = 1.89\%$. The major radius is $R_0 = 176(\text{cm})$. Both thermal and energetic ions are deuterium. Because the clearest electron cyclotron emission imaging (ECEI) data can be observed at 515 ms, and the background equilibrium does not change much during this short period (515 ms–528 ms),[19,34] we use the closest equilibrium data at $t = 525$ ms except for a global translation of the q value, where the $q_{\min}$ value is calculated from the fitted equation $q_{\min} = 4 - 0.004(t-528)$ with t in ms.

The boundary is assumed to be a perfect conducting wall. The choices of numerical parameters in simulations are based on convergence tests. We use 32 grid points in the parallel direction and 100 grid points in the radial direction. We keep the poloidal grid size approximately the same constant on different flux surfaces. Usually, we use 30–35 grid points in one poloidal wave length, with a grid size of about two thermal ion gyro-radii. The time step size is $\Delta t \approx 0.1R_0/v_{A0}$, where v_{A0} is the on-axis Alfvén speed. About 50 marker particles per cell are loaded for all species. The initial distribution of the marker particles is uniform in real space and Maxwellian in velocity space. A toroidal filter keeping only one toroidal mode number n is applied in the linear simulations. All poloidal harmonics are always kept.

A. Radial mode structures of stable TAE excited by antenna

First, we use artificial antennas to excite the weakly damped TAE (in the ideal MHD limit) by excluding EPs and suppressing all kinetic effects in GTC simulations.[31–33] The antenna profiles of the electrostatic potential ϕ are plotted in Fig. 1(a). The radial coordinate ρ in Fig. 1 is defined as $\rho \equiv \sqrt{\psi_{\text{tor}}/\psi_{tw}}$, with ψ_{tor} being the toroidal flux and ψ_{tw} being the toroidal flux at the separatrix. Several GTC simulations were carried out using antennas with different poloidal harmonic localized at their mode rational surfaces for the same toroidal mode number $\mathtt{n}=4$. Different combinations of antennas [listed in Fig. 1(b)] are loaded in different runs, but the resultant mode structures [shown also in Fig. 1(b)] and corresponding resonant frequencies are found to be

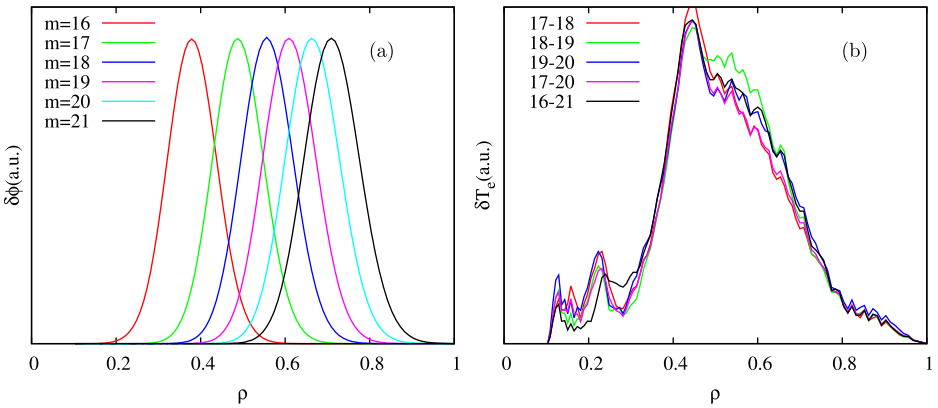

FIG. 1. (a) Electrostatic $\delta\phi$ antenna profile of different m-harmonics in different simulations. (b) Resultant δT_e profile excited by antennas with different m-harmonic combinations.

almost the same. This result confirms that the TAE in the MHD limit is a global eigenmode, which is insensitive to the location of the driving sources. It also confirms that perturbative drives can only drive the eigenmode without changing its mode structure or eigenfrequency.

Fig. 2 shows the radial structure of the radial displacement ξ_r of each m-harmonics for the $n=4$ TAE. Calculation from NOVA ideal MHD eigenmode code[50] is shown in panel (b). There are, in fact, hundreds of eigenmodes from NOVA calculation (Fig. 3). Considering both frequency and mode structure, we choose the eigenmode with 64 kHz (in the red box in Fig. 3) to be the best match to the ECE signal observed in the experiment. This eigenmode gives a stable TAE with a wide mode structure of $|\xi_r|$, which extends from $\rho \approx 0.4$ to $\rho \approx 0.9$ [Fig. 2(b)]. Note that there is a radial node in the mode structure from NOVA, i.e., this is not the ground eigenstate. The $|\xi_r|$ mode structure of antenna-driven stable TAE from GTC is plotted in Fig. 2(a), which also shows the global mode structure, but with no radial node (i.e., this is the ground eigenstate). The definition of radial displacement ξ_r in GTC is given in Appendix A. Panels (c)–(e) show the radial structures of EP-driven unstable TAEs with different EP drives. Details about these three panels will be discussed in Sec. III B.

Both GTC and NOVA show that the stable TAE has a global mode structure. However, there are some minor differences in the mode structures from these two models as shown in Figs. 2(a) and 2(b). There are several differences between these two models; thus, we do not expect their result to be exactly the same. For example, $\delta B_\parallel$ is ignored in GTC, but NOVA keeps that component. It is assumed that $k_\parallel \ll k_\perp$ in GTC simulations; however, NOVA formulation is not based on this assumption. There are also some differences in the Alfvén continuum as shown in Fig. 3 (NOVA) and Fig. 4 (GTC), which are due to the different geometry representations.

The frequency of the antenna-driven TAE from GTC is found to be 72 kHz, which is in good agreement with the experimental frequency at 69 kHz. The NOVA result of the TAE frequency is 64 kHz. The radial extent of the mode structure from GTC simulation with antenna excitation is similar to that calculated by NOVA. However, as we will show in Sec. III B, the mode structure of the unstable TAE

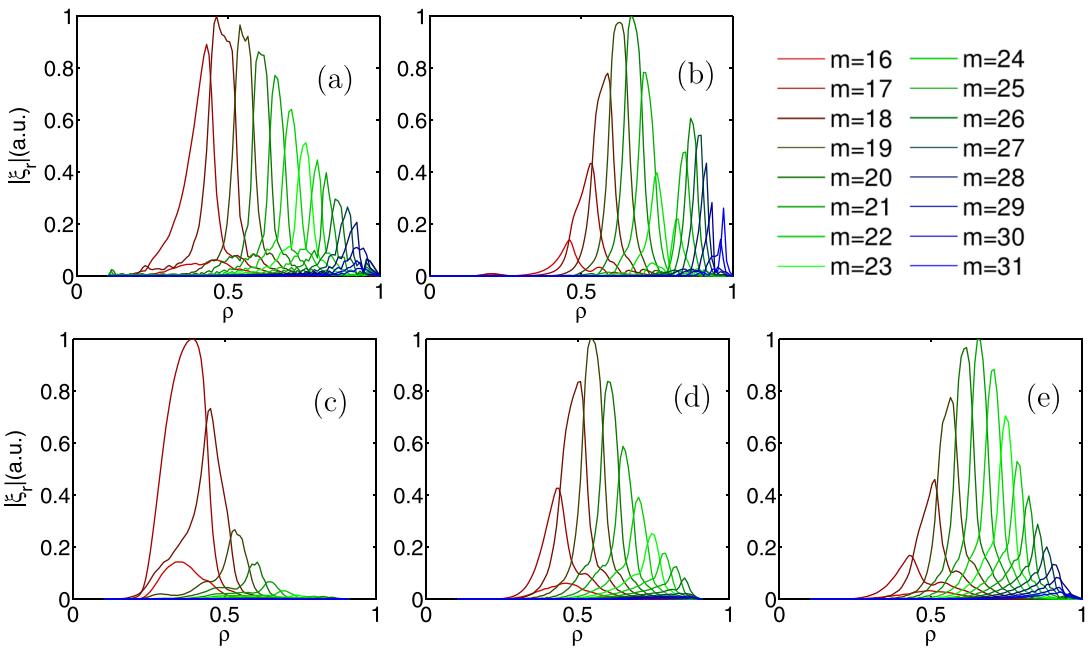

FIG. 2. Radial sturctures of the m-harmonics of the radial displacement ξ_r for the $n=4$ TAE from (a) GTC with antenna excitation, (b) NOVA ideal MHD eigenmode calculation, and GTC with EP drive in (c) case 1, (d) case 2, and (e) case 3 discussed in Sec. III B.

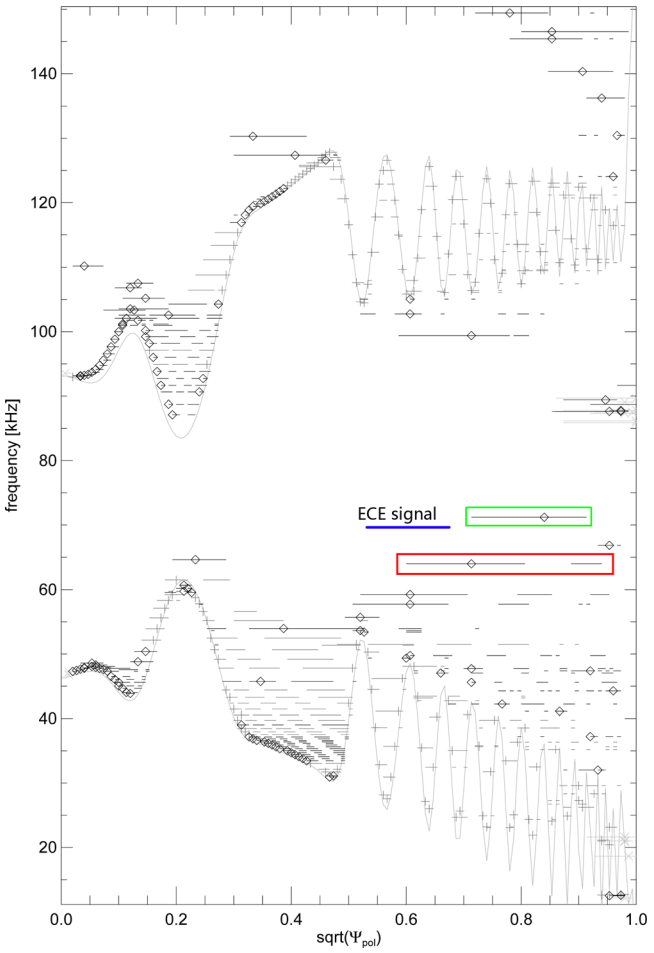

FIG. 3. All $n=4$ eigenmodes from NOVA calculation using the equilibrium profile in DIII-D discharge No. 142111 without toroidal flow. Blue line is the signal observed in the experiment. The eigenmode in red box has radial overlap with the experimental observation. The eigenmode in green box has no overlap with the experimental observation. The two lines in the red box indicate a single eigenmode with a radial node [Fig. 2(b)].

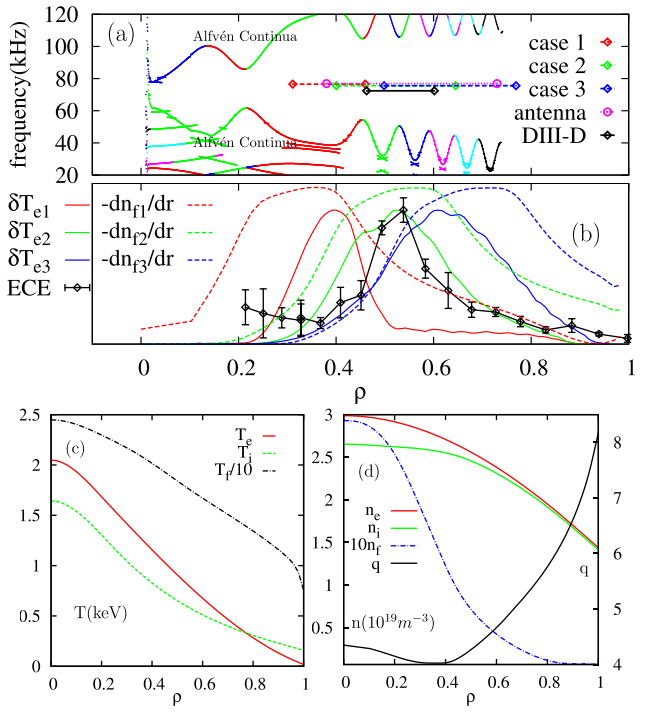

FIG. 4. (a) The frequencies (in the plasma frame) and radial locations (full width half maximum) of the simulated $n=4$ TAE with different EP density profiles in the Alfvén continua (calculated by ALCON [35]). (b) A comparison of the mode radial structures with their corresponding EP drives. The solid lines are the rms values of the relative electron temperature perturbation δT_e; The dashed lines are the EP density gradient dn_f/dr values. Different colors indicate different EP profiles in the simulation. The black solid line is the ECE data of δT_e from DIII-D. The last two panels from Ref. 40 show radial profiles of (c) temperature T, (d) density n and safety factor q of a DIII-D experiment (shot No. 142111 at 525 ms). Reprinted with permission from Z. Wang *et al.*, Phys. Rev. Lett. **111**, 145003 (2013). Copyright 2013 American Physical Society.

from GTC simulations with EP excitation is much narrower than the stable TAE from both GTC and NOVA.

B. Radial mode structure of unstable TAE excited by EP

Then EP drive is included in our following simulations. The EP profiles given by EFIT are shown in Figs. 4(c) and 4(d). The EP density gradient is much larger than the temperature gradient, and thus, the main drive of the instability. The TAE gap is very wide from both NOVA (Fig. 3) and ALCON (Fig. 4) calculations. The TAE eigen-frequency does not touch the continuum; thus, continuum damping is not important in this scenario. The best experimental measurement of TAE mode structure is at $t=515$ ms, so we set the $q_{\min}=4.052$ in our simulation to compare our results with experimental data. Because the simulation is run in the plasma frame but not the lab frame, a Doppler shift of (1.9n)kHz is substracted from experimental measurement when we compare the frequencies between simulation results and experimental results. Keeping only $n=4$ mode in our simulation, we can observe an unstable TAE if we use the EP profiles from EFIT. The TAE frequency and mode structure are shown in red lines in both panel (a) and panel (b) in Fig. 4. A direct comparison between experimental results (black lines) and simulation results can also be found in those two panels. Simulation agrees very well with experiment in terms of real frequency. However, the mode structures, especially the radial locations of TAE, are very different in simulation and in experiment.

To resolve this discrepancy, we decide to carry out a sensitivity test on the EP density profile, which is the most unreliable data from the experiment. In case 2 and case 3, plotted in Fig. 4, we use an EP density profile that shifts outward for 0.06 m and 0.10 m, respectively. The EP density gradients are shown in dashed lines in Fig. 4(b), and their resultant TAE mode structures are shown in solid lines in panel (b) and dashed lines in panel (a), with corresponding colors. In this scan of the EP density profile, we find that, contrary to the antenna-driven stable TAE, the radial position of the EP-driven unstable TAE is now strongly correlated with that of the strongest EP drive. This phenomenon is inconsistent with the prediction from the conventional MHD treatment of the Alfvén eigenmodes in which only perturbative EP contribution is added on top of the the thermal plasma described by the MHD framework.

The amplitudes of different m-harmonics in these three runs are also shown in panels (c)–(e) of Fig. 2. Each m-harmonic is always located around its own mode rational

surface, regardless of where the total mode structure peaks at. Three radial structures are all significantly narrower than either the radial structure of the antenna-driven TAE in GTC [Fig. 2(a)] or that of NOVA eigenmode [Fig. 2(b)].

Perturbative EP treatment will only give the eigenmode a finite growth rate without changing its eigen frequency or its mode structure from the ideal MHD theory. But, in our simulation, not only the EP-driven unstable TAE has a different mode structure from the antenna-driven stable TAE, but the mode structure can also change as a response to the change in EP drive as well. In fact, one of the important basic assumption for perturbative treatment for EP, $\beta_{EP} \ll \beta_{thermal}$, does not hold in the DIII-D experiments. So, we attribute this radial localization phenomenon to the non-perturbative EP contribution.

It could be argued that there are multiple TAEs in the TAE gap in the ideal MHD theory and their eigenfrequencies may have very small differences. However, GTC finds the same global eigenmode when using different antennas at various radial locations (Fig. 1). Furthermore, NOVA results show that in the frequency range of interest, there are only two relevant eigenmodes (the eigenmode in the red box and the eigenmode in the green box in Fig. 3) whose eigenfrequencies are different by over 7 kHz. The frequency resolution (half width of the resonance peak) is about 2 kHz in the antenna frequency scan in our simulation, so what we find by the antenna excitation in GTC is a single TAE eigenmode.

There are two other differences between simulation settings and experiments, but neither of them would be a reasonable explanation of the radial localization phenomenon. One factor is the sheared toroidal flow, which induces the flow shear effects and centrifugal force. Regarding the flow shear effect, we take it as negligible because the difference of flow across the whole mode width is only about 4 kHz compared to the 70 kHz frequency of TAE. Regarding the centrifugal force in a rotating frame, it is not likely that it will influence the results much because the parallel flow is much smaller than the phase velocity of the Alfvén wave and the thermal velocity of particles, $u_{\|}/v_A \ll u_{\|}/v_{th,i} \approx 5\%$. Another factor is the EP distribution function. Anisotropic slowing down distribution is often used as a more realistic distribution for fast ions generated by NBI. However, in this discharge, there are two NBIs both in co- and counter-directions of the toroidal current. The resultant distribution for EP should thus be closer to an isotropic distribution, which can be reasonably described by the Maxwellian distribution. Moreover, such treatments of rotation and EP distribution have already been successfully applied in the previous study,[19,34] which successfully recovers the reversed shear Alfvén eigenmode (RSAE) frequency upsweeping observed also in DIII-D discharge No. 142111. The simulation parameters in that study are very similar to the current study. In fact, it is just a different time window in the same DIII-D discharge.

In summary, we conclude that the non-perturbative EP contribution is the main reason for the radial localization of TAE, i.e., the EP-driven TAE has a radial mode width much smaller than that predicted by the MHD and that the TAE radial structure peaks at and moves with the location of the strongest EP pressure gradients. This explanation is also consistent with the radial outdrift of TAE mode structure found in this experiment.[40]

The fast-ion gradient is poorly constrained by the existing measurements (Fig. 5). One measurement of the fast-ion profile is obtained from the difference between the equilibrium total pressure and the thermal particle pressure. The random errors in the fast-ion pressure are readily estimated from the random errors in the electron and carbon densities, and electron and ion temperatures. However, systematic errors associated with the equilibrium reconstruction are difficult to quantify. The EFIT[48] procedure fits the pressure profile to a pre-specified functional form that effectively assumes a smoother gradient than the actual gradient. The second measurement of the fast-ion profile is from fast-ion D-alpha (FIDA) light.[51] (The "FIDA density" shown in Fig. 5 is the FIDA brightness after integration over wavelength divided by the injected neutral density.) The plotted error bars are from an ensemble of 9 time slices with nearly identical plasma parameters; although photon statistics and background variations contribute to these errors, it is likely that significant temporal variations in the actual fast-ion density also contribute. Both measurements show substantial flattening of the fast-ion profile relative to classical predictions, as previously reported.[52] Neither measurement provides sufficient spatial resolution to determine the fast-ion gradient. As shown in Fig. 5, within experimental error, the modelled pressure profile in case 2 is compatible with the data.

C. Radial shearing of TAE mode structure

Amongst these three simulations in Fig. 4, the resultant mode radial location from case 2 fits the ECE data the best. Therefore, all the following simulations have been carried out with the EP density profile in the case 2.

Contour plots of the $\delta\phi$ mode structure from both antenna-driven TAE and EP-driven TAE are shown in Fig. 6. Besides the obvious difference between the mode radial widths we mentioned in Sec. III B, the next major difference between antenna-driven stable TAE and EP-driven

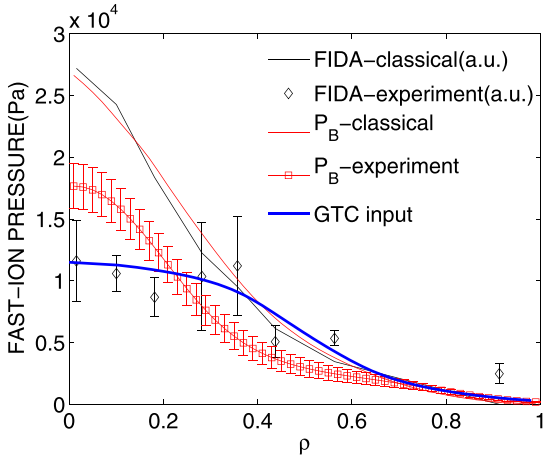

FIG. 5. Fast-ion pressure profile (black) and fast-ion density (red) vs. normalized minor radius at 525 ms. The solid lines show the classically predicted pressure (P_B as beam-ion pressure in the figure) and FIDA density profiles. The bold blue line indicates the EP pressure used as GTC input in case 2.

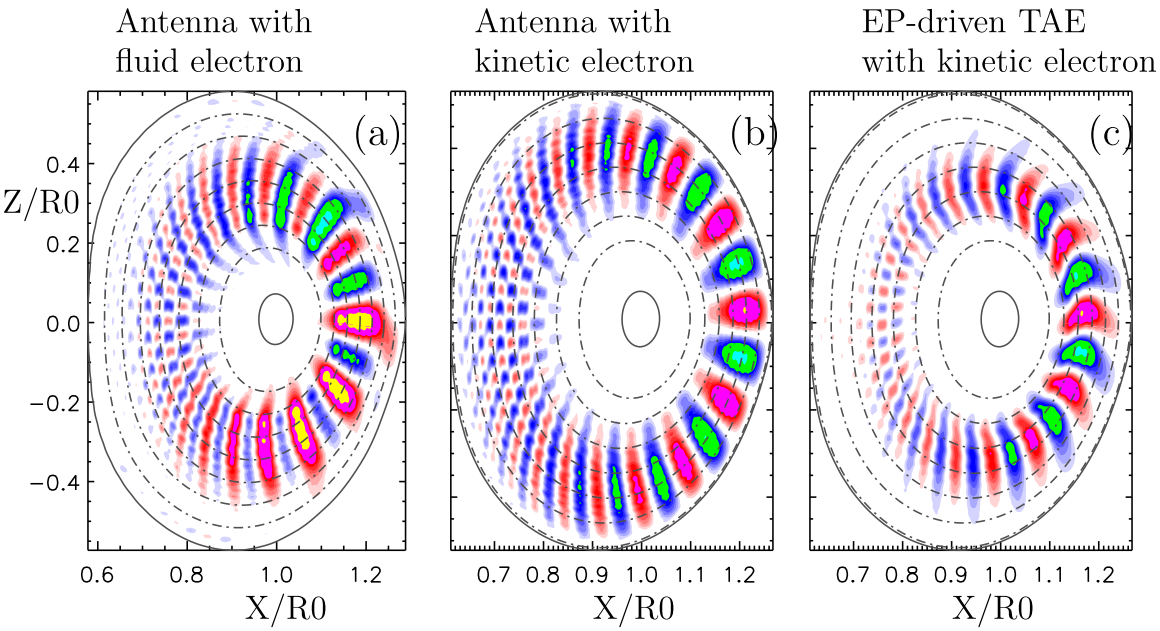

FIG. 6. Poloidal contour plot of electrostatic potential $\delta\phi$ from GTC simulation of (a) antenna-driven n = 4 TAE without kinetic electrons (b) antenna-driven n = 4 TAE with kinetic electrons (c) EP-driven n = 4 TAE eigenstructures with kinetic electrons.

unstable TAE is the radial-shearing of their mode structure. The antenna-driven TAE shows no radial phase shearing (i.e., Bloch phase shift is zero in the ballooning mode theory and the eigenmode can be described by Eq. (37)), which we refer to as the radial symmetry. When kinetic trapped electrons are included, the mode structure change from Figs. 6(a) and 6(b). Though the radial position changes, there is still little radial shearing. However, the EP-driven TAE [Fig. 6(c)] shows an obvious radial phase shearing. Apparently, the strong magnetic diamagnetic flow of EP breaks the radial symmetry and causes this radial phase shearing. This phenomenon, which has also been observed in the experiment[16] and other simulations,[19,31–34,36] illustrates that non-perturbative EP contribution can change the TAE mode structure significantly.

D. Poloidal asymmetry of wavelength

In both experiments and simulations, it is always observed that poloidal mode width is larger at the low field side, even for the mode dominated by a single poloidal mode number (e.g., RSAE). This phenomenon complicates the determination of the poloidal mode number in experiments.

The main reason for this poloidal asymmetry is that the unstable modes in magnetized plasma favour the condition $k_\perp \gg k_\parallel \approx 0$, because of the stabilization of the large-$k_\parallel$ modes by the field line bending effects. Therefore, the mode mostly aligns with the magnetic field line. In the high field side, the field lines are compressed, thus give the modes a smaller poloidal mode width.

To calculate the poloidal asymmetry of the poloidal wavelength, we consider a flux-tube connecting the high field side to the low field side. A volume element of $(\Delta\psi, \Delta\theta, \Delta\zeta)$ at the high (low) field side has a radial width Δr_i (Δr_o), a poloidal width $\Delta l_i^{(p)}$ ($\Delta l_o^{(p)}$), and a toroidal width $\Delta l_i^{(t)}$ ($\Delta l_o^{(t)}$). As we know, the Jacobian $\mathcal{J} = (gq + I)/B^2$ is proportional to the volume of a volume element $(\mathcal{J}\Delta\psi\Delta\theta\Delta\zeta)$. Because g, q, I are all flux functions in the magnetic coordinate, we know that on the same flux surface,

$$\frac{\Delta l_o^{(p)}}{\Delta l_i^{(p)}} \cdot \frac{\Delta r_o}{\Delta r_i} \cdot \frac{\Delta l_o^{(t)}}{\Delta l_i^{(t)}} = \frac{\mathcal{J}_o}{\mathcal{J}_i} = \left(\frac{B_i}{B_o}\right)^2 = \left(\frac{1+\epsilon}{1-\epsilon}\right)^2. \tag{49}$$

Here, we assume magnetic field intensity depending inversely on the major radius. The subscript o indicates outside (low-field side), i indicates inside (high-field side).

For a simple circular cross-section tokamak,

$$\frac{\Delta r_o}{\Delta r_i} = \frac{1-\Delta'}{1+\Delta'}, \quad \frac{\Delta l_o^{(t)}}{\Delta l_i^{(t)}} = \frac{R_o}{R_i} = \frac{1+\epsilon}{1-\epsilon}, \tag{50}$$

$$\text{so } \frac{\Delta l_o^{(p)}}{\Delta l_i^{(p)}} = \frac{\mathcal{J}_o}{\mathcal{J}_i}\frac{\Delta r_i}{\Delta r_o}\frac{\Delta l_i^{(t)}}{\Delta l_o^{(t)}} = \frac{1+\epsilon}{1-\epsilon}\cdot\frac{1+\Delta'}{1-\Delta'}, \tag{51}$$

where the Δ' is the derivative of Shafranov shift.[53] Δ' can either be measured directly from experimental data, or be calculated by

$$\Delta' = \left(\frac{L}{2} + \beta_\theta\right) r, \tag{52}$$

where $L = [2/(r^2 B_\theta^2)] \int_0^r B_\theta^2 r dr$ is the internal inductance per unit length, and $\beta_\theta = (2/B_\theta^2)(\bar{p} - p)$, with $\bar{p} = (2/r^2) \int_0^2 prdr$ the average pressure.

Now, we can compare this ratio from the theory with the GTC measurement for the m = 18 harmonic mode structure on the $q = 4.5$ flux surface (Fig. 7). The theoretical estimation using Eq. (51) is found to match simulation data very well. For the realistic flux surface in this case, we approximately calculate $\Delta = R_0 - (X_o + X_i)/2$ and $r = (X_o - X_i)/2$, where X_o is the outside intersection between the $q = 4.5$ flux surface with $Z = 0$ and X_i is the inside intersection. Using the EFIT

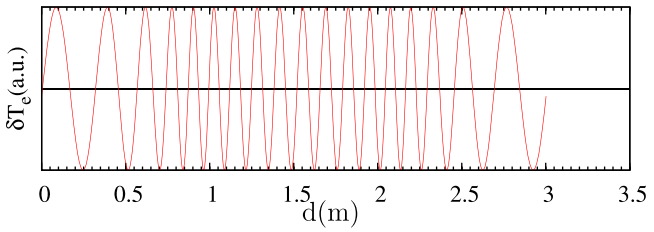

FIG. 7. δT_e mode structure of $\mathrm{n}=4$, $\mathrm{m}=18$ harmonics on $q=4.5$ flux surface. d is the poloidal distance on the $\zeta=0$ line of $q=4.5$ flux surface, measured from $\theta=0$ point in GTC simulation.

equilibrium data, ϵ and Δ' on the $q=4.5$ flux surface in this case are calculated by

$$\epsilon \equiv \frac{r}{R_0-\Delta} \approx 0.21, \quad \Delta' \equiv \frac{d\Delta}{dr} \approx 0.21. \tag{53}$$

So, the theoretical prediction of $\Delta l_o^{(p)}/\Delta l_i^{(p)}$ is:

$$\text{From theory (Eq. (51))}: \quad \frac{\Delta l_o^{(p)}}{\Delta l_i^{(p)}} \approx \frac{1.21}{0.79}\cdot\frac{1.21}{0.79} \approx 2.35. \tag{54}$$

This ratio measured from simulation (Fig. 7) is:

$$\text{From simulation}: \quad \frac{\Delta l_o^{(p)}}{\Delta l_i^{(p)}} \approx \frac{0.33m}{0.14m} \approx 2.36. \tag{55}$$

This method can serve as a useful tool to identify the poloidal mode number from experimental data like ECE image. In fact, the ECEI data of DIII-D shot No. 146101 (Ref. 54) from both the high-field-side window and the low-field-side window show a similar ratio of $\Delta l_o^{(p)}/\Delta l_i^{(p)} \approx 2$ for the RSAE mode structure with similar geometric parameters as shot 142111, but a smaller ϵ in the ECEI windows.

E. Frequency dependence on toroidal mode number

Now we extend our simulation to TAEs with other toroidal mode numbers. The results are summrized in Fig. 8. The frequencies plotted in this figure are all in the plasma frame. In the experiment, the three strong signals at $t=515$ ms are the $\mathrm{n}=3$ TAE with $f\approx 75$ kHz, the $\mathrm{n}=4$ TAE with $f\approx 80$ kHz, and the $\mathrm{n}=5$ TAE with $f\approx 85$ kHz.[55] Their frequencies, subtracted by their corresponding Doppler shifts, are also shown as black line in Fig. 8. The frequencies of the EP-driven TAEs in GTC (red line in Fig. 8) agree very well with those of the experimentally observed TAEs, all of which lie within the TAE gap in the

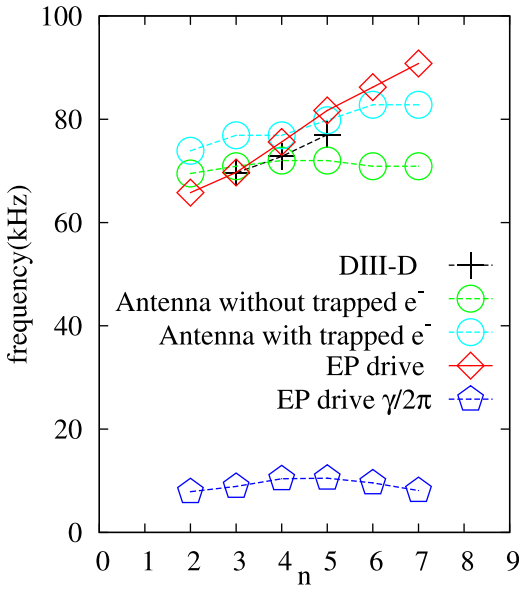

FIG. 8. Comparison of EP-driven unstable TAE frequencies and growth rates, antenna-driven stable TAE (with and without kinetic electrons) frequencies observed in simulations, with TAE frequencies observed in DIII-D experiments, as a function of toroidal mode number n in the plasma frame at $t=515$(ms). Adapted with permission from Z. Wang *et al.*, Phys. Rev. Lett. **111**, 145003 (2013). Copyright 2013 American Physical Society.

Alfvén continua. In fact, this consistency between simulation and experimental results can be further extended to the cases with different $q_{\min}$ values.[40] It is observed in both simulations and experiments that the TAE frequency does not change much as the $q_{\min}$ value is slowly decreasing.

The growth rates of the TAEs in GTC are shown as the blue curve in Fig. 8. We find the modes with the largest growth rates in simulations are $\mathrm{n}=3$–6. Considering that the nonlinear saturation level is usually lower for modes with higher-n, we can conclude that the modes with the largest growth rates in simulation agree qualitatively with the most dominant modes observed in the experiment ($\mathrm{n}=3$, 4, 5).

In the ideal MHD theory, the lowest order solution for TAE frequency should not depend on its toroidal mode number, as we demonstrated in Sec. II C. However, we can find that there is a frequency dependence on the toroidal mode number not only in the simulation results but also in the experiment even after we subtract the Doppler shift from the experimental results.

This deviation from the ideal MHD prediction should mainly be attributed to the non-perturbative EP contribution, i.e., the EP diamagnetic flow effects. The EP diamagnetic flow angular frequencies at the peak of the EP density gradients is

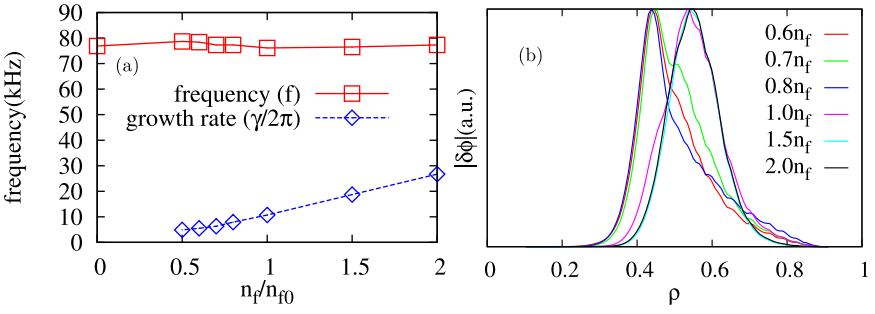

FIG. 9. (a) TAE frequencies and growth rates dependence on EP density. (b) Dominant mode structure dependence on the EP density.

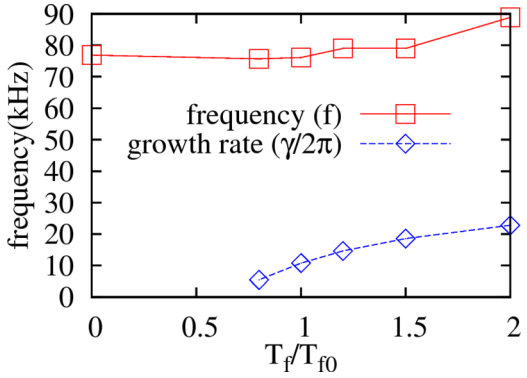

FIG. 10. TAE frequencies and growth rates dependence on EP temperature.

$$\omega^*_{EP} = k_\theta \frac{|\nabla P_f|}{eBn_f} \approx \frac{\mathrm{m}}{r}\frac{|\nabla\psi_p|}{eB_0 n_f}\frac{dP_f}{d\psi_p} = \frac{\mathrm{m}}{r}\frac{B_0 r|\nabla r|/q}{eB_0 n_f}\frac{dP_f}{d\psi_p}$$
$$= \frac{\mathrm{m}}{q}\frac{T_f}{e}\frac{d(P_f)}{P_f d\psi_p} = \frac{T_f}{e}\frac{d\ln(P_f)}{d\psi_p}\mathrm{n} = 4.97\times 10^5 \mathrm{n(rad/s)}, \tag{56}$$

so $\frac{1}{2\pi}\frac{n_f}{n_i}\omega^*_{EP} = 5\mathrm{n(kHz)}$. Therefore, the difference between the frequencies of TAEs with neighbouring n modes, about 4(kHz) in the experiments and 6(kHz) in the simulations, is about the same magnitude as the difference of their EP diamagnetic flow frequencies. Another support for our explanation of this frequency dependence comes from our simulation results of antenna-driven TAEs. If we exclude EP kinetic effects in our simulation, the resonant frequencies of antenna-driven TAEs (the green line in Fig. 8) are almost the same for n = 2–7. If we include trapped electron effects, we find that the resonant frequencies of antenna excitations are now higher for modes with higher-n numbers (the cyan line in Fig. 8). Finally, if we add EP in our simulation, the dependence of TAE frequency on the toroidal mode number becomes even stronger.

IV. DEPENDENCE OF GROWTH RATE ON EP DRIVE

In this section, we carry out a scan of fast ion density and temperature. We adopt all the input parameters in the case 2 of Sec. III, and then multiply the EP density and temperature with a constant factor from 0.5 to 2.0 in different simulations. The results are shown in Figs. 9–11. The data points of $n_f = 0$ and $T_f = 0$ use the resonance frequency from antenna excitation. n_{f0} and T_{f0} denote the equilibrium density and temperature of fast ions respectively.

In both scans, the frequencies remain roughly constant, while the growth rates increase with the EP pressure. The constant frequencies indicate that what we observe is still a TAE rather than an EPM, whose frequency depends on the EP transit/bounce frequencies. However, the frequency only goes up slightly when the EP temperature is increased by a factor of two. From the right panel of Fig. 9, we can see a clear shift from an eigenmode structure peaking at $\rho \approx 0.52$ in the strong drive cases to another eigenmode structure peaking at $\rho \approx 0.44$ in the weak drive cases. These two modes, though have very different mode structures, have very similar frequencies independent of the EP density. The dependence of the growth rates of these two modes on the EP density can both be fitted well to a linear relation, intersecting at some point between $0.8n_f$ to $1.0n_f$. A linear fit of the growth rate versus EP density shows that the mode closer to the separatrix has a threshold of $0.3n_f$. The other mode closer to the axis, however, has almost no threshold. We can only observe the most unstable mode in different parameter regimes in GTC, thus causing the sudden shift of the dominant mode structure with the gradual EP density increase. This shift of the most unstable mode structure is also illustrated in Fig. 11. The mode structures shown in panel (a) and (b) are quite similar, so are the ones shown in panel (c) and (d). However, the mode structures on the left peak closer to the axis. Such a mode shift is also observed in the EP temperature scan.

V. CONCLUSION

In conclusion, GTC linear simulations recover TAEs observed in DIII-D shot No. 142111 at 525 ms. Agreement between simulations and experiments in both frequency and mode structure is in a reasonable range, if we modify the EP density profile within experimental uncertainty. We find the dependence of TAE radial location on the EP drive profile. Antenna excitation results show a wider mode structure for the TAE from GTC, which is very similar to the ideal MHD

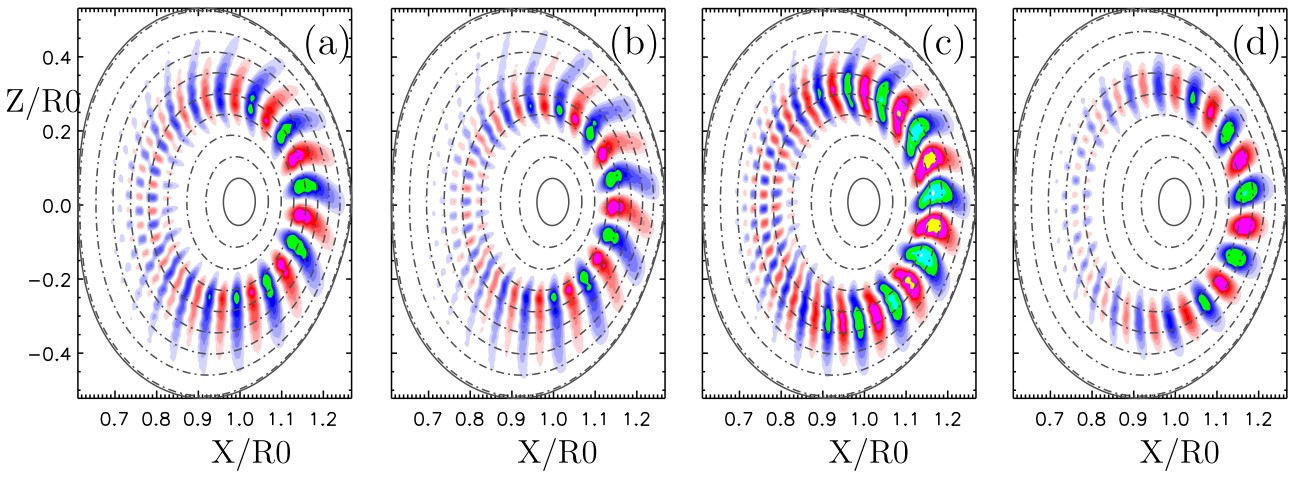

FIG. 11. The electrostatic potential $\delta\phi$ mode structure of EP-driven TAE with the original EP density times a factor of (a) 0.6, (b) 0.7, (c) 1.0, (d) 2.0.

eigenmode from NOVA. This suggests that the localization should be attributed to EP non-perturbative contributions. We find the radial and poloidal asymmetry in the TAE mode structure. Then we develop a method to estimate the poloidal mode number in the presence of the poloidal asymmetry. Kinetic effects, including trapped electron and kinetic EP, are found to introduce a dependence of the TAE frequency on the toroidal mode number. Scans of the EP pressure show a sudden shift of dominant mode structure when the EP pressure is reduced to a certain value.

ACKNOWLEDGMENTS

This work was supported by the U.S. Department of Energy (DOE) SciDAC GSEP center and by China National Magnetic Confinement Fusion Science Program, Grant No.2013GB111000. This research used resources of the Oak Ridge Leadership Computing Facility at Oak Ridge National Laboratory (DOE Contract No. DE-AC05-00OR22725), and the National Energy Research Scientific Computing Center (DOE Contract No. DE-AC02-05CH11231).

APPENDIX A: CALCULATING ξ_r IN GTC

In order to compare GTC results with NOVA results, first we need to compare the same variable. The mode structure from NOVA is presented by the radial component $\xi_r \equiv \boldsymbol{\xi}\cdot\nabla\psi$ (Ref. 50) (Their original notation is ξ_ψ. However, we use the symbol ξ_r here not to be confused with the covariant and contravariant notations used in this section).

The field equations in NOVA and GTC are

$$\begin{aligned}\text{NOVA}: &\begin{cases}\delta\boldsymbol{B}=\nabla\times(\boldsymbol{\xi}\times\boldsymbol{B}_0)\\ \delta\boldsymbol{E}=-\partial_t\boldsymbol{\xi}\times\boldsymbol{B}_0,\end{cases}\\ \text{GTC}: &\begin{cases}\delta\boldsymbol{B}=\nabla\times(\delta A_\parallel\boldsymbol{b}_0)\\ \delta\boldsymbol{E}=-\nabla\delta\phi-\partial_t\delta A_\parallel\boldsymbol{b}_0,\end{cases}\end{aligned} \tag{A1}$$

where $\delta E_\parallel=-\nabla_\parallel\delta\phi-\partial_t\delta A_\parallel=0$ is enforced in the ideal MHD limit of GTC. It is shown in Ref. 31 that these two frameworks are equivalent, so these two expressions should only be different in the choice of the gauge function. Now we define a gauge function (Eq. (A2)). $F(\boldsymbol{X},t)$ should satisfy the following relation (Eq. (A3)), so that the GTC expression can match exactly the MHD expression used in NOVA with a change of gauge (Eq. (A4)).

$$F(\boldsymbol{X},t)\equiv\int_0^t\delta\phi(\boldsymbol{X},t')dt' \tag{A2}$$

satisfies this relation:

$$\boldsymbol{\xi}\times\boldsymbol{B}_0=\nabla F+\delta A_\parallel\boldsymbol{b}_0, \tag{A3}$$

then the GTC expression of fields matches exactly the MHD expression of the fields

$$\begin{cases}\delta\boldsymbol{B}=\nabla\times(\delta A_\parallel\boldsymbol{b}_0)=\nabla\times(\delta A_\parallel\boldsymbol{b}_0+\nabla F)=\nabla\times(\boldsymbol{\xi}\times\boldsymbol{B}_0)\\ \delta\boldsymbol{E}=-\nabla\delta\phi-\partial_t\delta A_\parallel\boldsymbol{b}_0=-\partial_t(\delta A_\parallel\boldsymbol{b}_0+\nabla F)=-\partial_t\boldsymbol{\xi}\times\boldsymbol{B}_0.\end{cases} \tag{A4}$$

Thus, the perpendicular component of the ideal MHD displacement $\boldsymbol{\xi}_\perp$ can be calculated as

$$\begin{aligned}\boldsymbol{\xi}_\perp&=(\boldsymbol{B}_0\times\nabla F)/B_0^2=(\delta\nabla\psi+I\nabla\theta+g\nabla\zeta)\times\nabla F/B_0^2\\&=(I\partial_\zeta F-g\partial_\theta F)\frac{\boldsymbol{e}_\psi}{\mathcal{J}B_0^2}+g\partial_\psi F\frac{\boldsymbol{e}_\theta}{\mathcal{J}B_0^2}-I\partial_\psi F\frac{\boldsymbol{e}_\zeta}{\mathcal{J}B_0^2}\end{aligned} \tag{A5}$$

in GTC; if we neglect $\delta\nabla\psi$, the radial component of the equilibrium magnetic field in Boozer coordinates. Here, $\mathcal{J}\equiv[(\nabla\psi\times\nabla\theta)\cdot\nabla\zeta]^{-1}=(gq+I)/B_0^2$ is the Jacobian. $\boldsymbol{e}_\psi$, $\boldsymbol{e}_\theta$, $\boldsymbol{e}_\zeta$ are the covariant basis vectors defined as

$$\boldsymbol{e}_\psi\equiv\frac{\nabla\theta\times\nabla\zeta}{(\nabla\psi\times\nabla\theta)\cdot\nabla\zeta}=\mathcal{J}(\nabla\theta\times\nabla\zeta), \tag{A6}$$

$$\boldsymbol{e}_\theta\equiv\frac{\nabla\zeta\times\nabla\psi}{(\nabla\psi\times\nabla\theta)\cdot\nabla\zeta}=\mathcal{J}(\nabla\zeta\times\nabla\psi), \tag{A7}$$

$$\boldsymbol{e}_\zeta\equiv\frac{\nabla\psi\times\nabla\theta}{(\nabla\psi\times\nabla\theta)\cdot\nabla\zeta}=\mathcal{J}(\nabla\psi\times\nabla\theta). \tag{A8}$$

So, the contravariant expression of $\boldsymbol{\xi}_\perp$ is given by

$$\begin{aligned}\boldsymbol{\xi}_\perp&=\xi^\psi\boldsymbol{e}_\psi+\xi^\theta\boldsymbol{e}_\theta+\xi^\zeta\boldsymbol{e}_\zeta\\&=\frac{I\partial_\zeta F-g\partial_\theta F}{gq+I}\boldsymbol{e}_\psi+\frac{g\partial_\psi F}{gq+I}\boldsymbol{e}_\theta-\frac{I\partial_\psi F}{gq+I}\boldsymbol{e}_\zeta.\end{aligned} \tag{A9}$$

Then the radial component of displacement is

$$\xi_r=\boldsymbol{\xi}\cdot\nabla\psi=\boldsymbol{\xi}_\perp\cdot\nabla\psi=\xi^\psi=\frac{I\partial_\zeta F-g\partial_\theta F}{gq+I}, \tag{A10}$$

where the gauge function F is defined in Eq. (A2).

[1]C. Z. Cheng, L. Chen, and M. S. Chance, "High-n ideal and resistive shear Alfvén waves in tokamaks," Ann. Phys. **161**(1), 21–47 (1985).
[2]C. Z. Cheng and M. S. Chance, "Low-n shear Alfvén spectra in axisymmetric toroidal plasmas," Phys. Fluids **29**(11), 3695–3701 (1986).
[3]W. W. Heidbrink, E. J. Strait, M. S. Chu, and A. D. Turnbull, "Observation of beta-induced Alfvén eigenmodes in the DIII-D tokamak," Phys. Rev. Lett. **71**, 855–858 (1993).
[4]W. W. Heidbrink, E. Ruskov, E. M. Carolipio, J. Fang, M. A. van Zeeland, and R. A. James, "What is the "beta-induced Alfvén eigenmode?," Phys. Plasmas **6**(4), 1147–1161 (1999).
[5]L. Chen, "Theory of magnetohydrodynamic instabilities excited by energetic particles in tokamaks," Phys. Plasmas **1**(5), 1519–1522 (1994).
[6]G. Y. Fu and J. W. Van Dam, "Excitation of the toroidicity-induced shear Alfvén eigenmode by fusion alpha particles in an ignited tokamak," Phys. Fluids B **1**(10), 1949–1952 (1989).
[7]W. W. Heidbrink, E. J. Strait, E. Doyle, G. Sager, and R. T. Snider, "An investigation of beam driven Alfvén instabilities in the DIII-D tokamak," Nucl. Fusion **31**(9), 1635 (1991).
[8]K. L. Wong, R. J. Fonck, S. F. Paul, D. R. Roberts, E. D. Fredrickson, R. Nazikian, H. K. Park, M. Bell, N. L. Bretz, R. Budny, S. Cohen, G. W. Hammett, F. C. Jobes, D. M. Meade, S. S. Medley, D. Mueller, Y. Nagayama, D. K. Owens, and E. J. Synakowski, "Excitation of toroidal Alfvén eigenmodes in TFTR," Phys. Rev. Lett. **66**, 1874–1877 (1991).
[9]G. Manfredi and R. O. Dendy, "Test-particle transport in strong electrostatic drift turbulence with finite Larmor radius effects," Phys. Rev. Lett. **76**, 4360–4363 (1996).
[10]W. Zhang, Z. Lin, and L. Chen, "Transport of energetic particles by microturbulence in magnetized plasmas," Phys. Rev. Lett. **101**, 095001 (2008).
[11]W. Zhang, Z. Lin, and L. Chen, "Comment on "Electrostatic and magnetic transport of energetic ions in turbulent plasmas"," Phys. Rev. Lett. **107**, 239501 (2011).

[12]W. W. Heidbrink and G. J. Sadler, "The behaviour of fast ions in tokamak experiments," Nucl. Fusion **34**(4), 535 (1994).
[13]W. W. Heidbrink, J. M. Park, M. Murakami, C. C. Petty, C. Holcomb, and M. A. Van Zeeland, "Evidence for fast-ion transport by microturbulence," Phys. Rev. Lett. **103**, 175001 (2009).
[14]D. C. Pace, M. E. Austin, E. M. Bass, R. V. Budny, W. W. Heidbrink, J. C. Hillesheim, C. T. Holcomb, M. Gorelenkova, B. A. Grierson, D. C. McCune, G. R. McKee, C. M. Muscatello, J. M. Park, C. C. Petty, T. L. Rhodes, G. M. Staebler, T. Suzuki, M. A. Van Zeeland, R. E. Waltz, G. Wang, A. E. White, Z. Yan, X. Yuan, and Y. B. Zhu, "Energetic ion transport by microturbulence is insignificant in tokamaks," Phys. Plasmas **20**(5), 056108 (2013).
[15]K. Shinohara, Y. Kusama, M. Takechi, A. Morioka, M. Ishikawa, N. Oyama, K. Tobita, T. Ozeki, S. Takeji, S. Moriyama, T. Fujita, T. Oikawa, T. Suzuki, T. Nishitani, T. Kondoh, S. Lee, M. Kuriyama, JT-60 Team, G. J. Kramer, N. N. Gorelenkov, R. Nazikian, C. Z. Cheng, G. Y. Fu, and A. Fukuyama, "Alfvén eigenmodes driven by Alfvénic beam ions in JT-60U," Nucl. Fusion **41**(5), 603 (2001).
[16]B. J. Tobias, I. G. J. Classen, C. W. Domier, W. W. Heidbrink, N. C. Luhmann, R. Nazikian, H. K. Park, D. A. Spong, and M. A. Van Zeeland, "Fast ion induced shearing of 2D Alfvén eigenmodes measured by electron cyclotron emission imaging," Phys. Rev. Lett. **106**, 075003 (2011).
[17]M. Podest, R. E. Bell, A. Bortolon, N. A. Crocker, D. S. Darrow, A. Diallo, E. D. Fredrickson, G.-Y. Fu, N. N. Gorelenkov, W. W. Heidbrink, G. J. Kramer, S. Kubota, B. P. LeBlanc, S. S. Medley, and H. Yuh, "Study of chirping toroidicity-induced Alfvén eigenmodes in the national spherical torus experiment," Nucl, Fusion **52**(9), 094001 (2012).
[18]Ph. Lauber, I. G. J. Classen, D. Curran, V. Igochine, B. Geiger, S. da Graa, M. Garca-Muoz, M. Maraschek, P. McCarthy, and ASDEX Upgrade Team, "NBI-driven Alfvénic modes at ASDEX Upgrade," Nucl. Fusion **52**(9), 094007 (2012).
[19]D. A. Spong, E. M. Bass, W. Deng, W. W. Heidbrink, Z. Lin, B. Tobias, M. A. Van Zeeland, M. E. Austin, C. W. Domier, and N. C. Luhmann, Jr., "Verification and validation of linear gyrokinetic simulation of Alfvén eigenmodes in the DIII-D tokamak," Phys. Plasmas **19**(8), 082511 (2012).
[20]Ph. Lauber, S. Gunter, and S. D. Pinches, "Kinetic properties of shear Alfvén eigenmodes in tokamak plasmas," Phys. Plasmas **12**(12), 122501 (2005).
[21]Ph. Lauber, S. Gnter, A. Knies, and S. D. Pinches, "Ligka: A linear gyrokinetic code for the description of background kinetic and fast particle effects on the mhd stability in tokamaks," J. Comput. Phys. **226**(1), 447–465 (2007).
[22]J. Lang, Y. Chen, S. E. Parker, and G.-Y. Fu, "Gyrokinetic delta f particle simulations of toroidicity-induced Alfvén eigenmode," Phys. Plasmas **16**(10), 102101 (2009).
[23]Y. Chen, S. E. Parker, J. Lang, and G.-Y. Fu, "Linear gyrokinetic simulation of high-n toroidal Alfvén eigenmodes in a burning plasma," Phys. Plasmas **17**(10), 102504 (2010).
[24]A. Mishchenko, R. Hatzky, and A. Konies, "Global particle-in-cell simulations of Alfvénic modes," Phys. Plasmas **15**(11), 112106 (2008).
[25]A. Mishchenko, A. Konies, and R. Hatzky, "Global particle-in-cell simulations of fast-particle effects on shear Alfvén waves," Phys. Plasmas **16**(8), 082105 (2009).
[26]E. M. Bass and R. E. Waltz, "Gyrokinetic simulations of mesoscale energetic particle-driven Alfvénic turbulent transport embedded in microturbulence," Phys. Plasmas **17**(11), 112319 (2010).
[27]E. M. Bass and R. E. Waltz, "Gyrokinetic simulation of global and local Alfvén eigenmodes driven by energetic particles in a DIII-D discharge," Phys. Plasmas **20**(1), 012508 (2013).
[28]Z. Lin, T. S. Hahm, W. W. Lee, W. M. Tang, and R. B. White, "Turbulent transport reduction by zonal flows: Massively parallel simulations," Science **281**(5384), 1835–1837 (1998).
[29]Z. Lin, I. Holod, L. Chen, P. H. Diamond, T. S. Hahm, and S. Ethier, "Wave-particle decorrelation and transport of anisotropic turbulence in collisionless plasmas," Phys. Rev. Lett. **99**, 265003 (2007).
[30]Y. Xiao and Z. Lin, "Convective motion in collisionless trapped electron mode turbulence," Phys. Plasmas **18**(11), 110703 (2011).
[31]W. Deng, Z. Lin, I. Holod, X. Wang, Y. Xiao, and W. Zhang, "Gyrokinetic particle simulations of reversed shear Alfvén eigenmode excited by antenna and fast ions," Phys. Plasmas **17**(11), 112504 (2010).
[32]H. S. Zhang, Z. Lin, I. Holod, X. Wang, Y. Xiao, and W. L. Zhang, "Gyrokinetic particle simulation of beta-induced Alfvén eigenmode," Phys. Plasmas **17**(11), 112505 (2010).
[33]W. Zhang, I. Holod, Z. Lin, and Y. Xiao, "Global gyrokinetic particle simulation of toroidal Alfvén eigenmodes excited by antenna and fast ions," Phys. Plasmas **19**(2), 022507 (2012).
[34]W. Deng, Z. Lin, I. Holod, Z. Wang, Y. Xiao, and H. Zhang, "Linear properties of reversed shear Alfvén eigenmodes in the DIII-D tokamak," Nucl. Fusion **52**(4), 043006 (2012).
[35]W. Deng, Z. Lin, and I. Holod, "Gyrokinetic simulation model for kinetic magnetohydrodynamic processes in magnetized plasmas," Nucl. Fusion **52**(2), 023005 (2012).
[36]H. S. Zhang, Z. Lin, and I. Holod, "Nonlinear frequency oscillation of Alfvén eigenmodes in fusion plasmas," Phys. Rev. Lett. **109**, 025001 (2012).
[37]H. S. Zhang, Z. Lin, W. Deng, I. Holod, Z. X. Wang, Y. Xiao, and W. L. Zhang, "Nonlinear dynamics of beta-induced Alfvén eigenmode in tokamak," Phys. Plasmas **20**(1), 012510 (2013).
[38]Y. Nishimura, "Excitation of low-n toroidicity induced Alfvén eigenmodes by energetic particles in global gyrokinetic tokamak plasmas," Phys. Plasmas **16**(3), 030702 (2009).
[39]C. Zhang, W. Zhang, Z. Lin, and D. Li, "Comparison of toroidicity-induced Alfvén eigenmodes and energetic particle modes by gyrokinetic particle simulations," Phys. Plasmas **20**(5), 052501 (2013).
[40]Z. Wang, Z. Lin, I. Holod, W. W. Heidbrink, B. Tobias, M. Van Zeeland, and M. E. Austin, "Radial localization of toroidicity-induced Alfvén eigenmodes," Phys. Rev. Lett. **111**, 145003 (2013).
[41]F. Zonca, S. Briguglio, L. Chen, G. Fogaccia, and G. Vlad, "Transition from weak to strong energetic ion transport in burning plasmas," Nucl. Fusion **45**(6), 477 (2005).
[42]A. J. Brizard and T. S. Hahm, "Foundations of nonlinear gyrokinetic theory," Rev. Mod. Phys. **79**, 421–468 (2007).
[43]W. W. Lee, "Gyrokinetic particle simulation model," J. Comput. Phys. **72**(1), 243–269 (1987).
[44]I. Holod, W. L. Zhang, Y. Xiao, and Z. Lin, "Electromagnetic formulation of global gyrokinetic particle simulation in toroidal geometry," Phys. Plasmas **16**(12), 122307 (2009).
[45]Z. Lin and L. Chen, "A fluid–kinetic hybrid electron model for electromagnetic simulations," Phys. Plasmas **8**(5), 1447–1450 (2001).
[46]L. Chen and F. Zonca, "Theory of shear Alfvén waves in toroidal plasmas," Phys. Scr. **1995**(T60), 81.
[47]L. Chen, "Alfvén waves: A journey between space and fusion plasmas," Plasma Phys. Controlled Fusion **50**(12), 124001 (2008).
[48]L. L. Lao, H. St. John, R. D. Stambaugh, A. G. Kellman, and W. Pfeiffer, "Reconstruction of current profile parameters and plasma shapes in tokamaks," Nucl. Fusion **25**(11), 1611 (1985).
[49]W. W. Pfeiffer, R. H. Davidson, R. W. Miller, and R. E. Waltz, "Onetwo: A computer code for modeling plasma transport in tokamaks," General Atomics Report No. GA-A16178, 1980.
[50]C. Z. Cheng and M. S. Chance, "Nova: A nonvariational code for solving the MHD stability of axisymmetric toroidal plasmas," J. Comput. Phys. **71**(1), 124–146 (1987).
[51]W. W. Heidbrink, N. N. Gorelenkov, Y. Luo, M. A. Van Zeeland, R. B. White, M. E. Austin, K. H. Burrell, G. J. Kramer, M. A. Makowski, G. R. McKee, and R. Nazikian, "Anomalous flattening of the fast-ion profile during Alfvén-eigenmode activity," Phys. Rev. Lett. **99**, 245002 (2007).
[52]W. W. Heidbrink, "Fast-ion d measurements of the fast-ion distribution (invited)a)," Rev. Sci. Instrum. **81**(10), 10D727 (2010).
[53]R. B. White, *The Theory of Toroidally Confined Plasmas*, 2nd edition ed. (Imperial College Press, 2006).
[54]B. Tobias, E. M. Bass, I. G. J. Classen, C. W. Domier, B. A. Grierson, W. W. Heidbrink, N. C. Luhmann, Jr., R. Nazikian, H. K. Park, D. A. Spong, and M. A. Van Zeeland, "Alfvén eigenmode structure during off-axis neutral beam injection," Nucl. Fusion **52**(10), 103009 (2012).
[55]M. A. Van Zeeland, N. N. Gorelenkov, W. W. Heidbrink, G. J. Kramer, D. A. Spong, M. E. Austin, R. K. Fisher, M. Garca Muoz, M. Gorelenkova, N. Luhmann, M. Murakami, R. Nazikian, D. C. Pace, J. M. Park, B. J. Tobias, and R. B. White, "Alfvén eigenmode stability and fast ion loss in DIII-D and ITER reversed magnetic shear plasmas," Nucl. Fusion **52**(9), 094023 (2012).